applied sciences

MDPI

Article

Detectability of Subsurface Defects in Polypropylene/Glass Fiber Composites Using Multiple Lock-In Frequency Modulated Algorithms

Yoonjae Chung [1], Seungju Lee [2], Ranjit Shrestha [3] and Wontae Kim [4,*]

[1] Eco-Sustainable Energy Research Institute, Kongju National University, 1223-24 Cheonan-daero, Cheonan-si 31080, Republic of Korea
[2] Department of Future Convergence Engineering, Kongju National University, 1223-24 Cheonan-daero, Cheonan-si 31080, Republic of Korea
[3] Department of Mechanical Engineering, School of Engineering, Kathmandu University, Kathmandu P.O. Box 6250, Nepal
[4] Division of Mechanical & Automotive Engineering, Kongju National University, 1223-24 Cheonan-daero, Cheonan-si 31080, Republic of Korea
* Correspondence: kwt@kongju.ac.kr; Tel.: +82-41-521-9289

Abstract: Recently, thermographic testing has been applied as a non-destructive evaluation technology for composite materials due to its remarkable advantages, such as its non-contact, non-destructive, and high-speed properties, it is harmless to the human body and easy to use, as well as having both qualitative and quantitative inspection performance. In this paper, multiple lock-in frequency modulated thermography is applied to investigate defects on the subsurface of polypropylene/glass fiber composites, and experimental investigations were conducted on various defect conditions for qualitative and quantitative estimation. A thin rectangle-shaped PP-GF plate of dimension 100 × 180 mm and a depth of 3 mm with various 24 defects conditions was considered as a test sample. The sample was stimulated at multiple modulation frequencies, viz., 1 Hz, 0.2 Hz, 0.1 Hz, 0.05 Hz, 0.03 Hz, and 0.01 Hz. For qualitative and quantitative evaluation, two representatives, multiple lock-in frequency modulated algorithms of lock-in thermography, HA and FFT, were applied to the raw data. Moreover, their detectability performance was compared in terms of phase contrast and signal-to-noise ratio.

Keywords: polypropylene/glass fiber composites; lock-in thermography; multi frequency approach; phase contrast; signal-to-noise ratio

check for updates

Citation: Chung, Y.; Lee, S.; Shrestha, R.; Kim, W. Detectability of Subsurface Defects in Polypropylene/Glass Fiber Composites Using Multiple Lock-In Frequency Modulated Algorithms. *Appl. Sci.* **2023**, *13*, 545. https://doi.org/10.3390/app13010545

Academic Editor: Piervincenzo Rizzo

Received: 9 November 2022
Revised: 21 December 2022
Accepted: 27 December 2022
Published: 30 December 2022

Copyright: © 2022 by the authors. Licensee MDPI, Basel, Switzerland. This article is an open access article distributed under the terms and conditions of the Creative Commons Attribution (CC BY) license (https://creativecommons.org/licenses/by/4.0/).

1. Introduction

Recently, the use of fiber-reinforced composites to replace steel materials for weight reduction in various industrial fields has grown rapidly. Fiber-reinforced composites are expected to continue to be utilized due to their excellent specific strength and stiffness [1]. Thermoplastic composites are popular due to their low cost, easy maintenance and recyclability, good damage resistance, impact and fracture toughness, and resistance to microcracks [2]. One of the thermoplastic composites includes polypropylene. One of the most important applications of organic reinforced polypropylene is in the aeronautical and automotive industries using inexpensive molding techniques. It is used in major components, panels, doors, etc. [3].

Glass-reinforced polypropylene (PP-GF) can be affected by voids, peeling, cracks, bonding defects, and manufacturing process defects due to foreign substances, including volatile resin components. In addition, defects, such as fiber damage, cracks, water penetration, and impact damage, can be generated [4]. Non-destructive testing (NDT) is a wide group of testing and analysis techniques used in science and industry to evaluate the properties of a material, structure, or system for characteristic defects and discontinuities without damage [5]. Generally, visual inspection (VI), ultrasonic inspection (UT),

radiographic inspection (RT), and acoustic emission (AE) techniques have been used as non-destructive testing techniques for polypropylene composites. However, each technique has problems and needs improvement [6,7]. UT is the most widely used technology for control and non-destructive inspection in various industrial fields, such as internal defect detection of composite materials, power generation turbine plates, nuclear power plant components, ships, autonomous aircraft structures, automobile parts, etc. In previous research, studies on the shape, size, location, and depth quantification of various types of defects were conducted using A-scan and C-scan UT techniques [8,9]. However, there are limitations in the narrow inspection area, long inspection time, and difficulty in accessing complex structures. RT is widely used mainly for the detection of discontinuities and defects in materials. However, special considerations are required when a specific material, such as a polymer with low X-ray attenuation coefficients, is scanned. Through many previous studies, X-ray CT was used to detect various types of defects and to characterize composite materials and structures [10,11]. VI is only effective at detecting macroscopic defects, such as poor surface finish and poor bonding. AE takes a long time to process and analyze data and requires specific skills and experience [12,13]. In this context, infrared thermography (IRT) can be used as an alternative technology and has the advantage of being able to inspect a large area quickly without contact and destructiveness.

Recently, IRT has been of the promising technologies and has been applied in various fields of application [14–16]. Moreover, thermographic testing has proved to be a valuable approach for non-destructive testing and evaluation of the structural stability of materials. Figure 1 shows the classification of approaches of IRT non-destructive testing methods. IRT is classified into two approaches: passive thermography and active thermography, as shown in Figure 1. In passive thermography, no external energy is used to stimulate the thermal gradients at the target's surface being tested [17]. The principle is that a temperature gradient is naturally generated by self-heating. Active thermography maximizes the temperature difference between defects and sound areas by heating the sample surface through an external excitation source [18]. A variety of external energy sources can be used for active thermography, for example optical excitation (halogen lamp, flash lamp, laser), eddy current, ultrasound, and others [19]. In addition, the heating energy can be applied in a harmonic form, pulsed form, or step-heated form [20,21]. When a sample is heated or cooled, heat propagates by diffusion through the material, which directly affects the temporal behavior of the surface temperature. Then, the thermal response of the investigated object, recorded by the infrared camera, is observed to reveal the presence of the defect. When a test target is heated by incident thermal energy, heat propagates by diffusion through the material, which directly affects the temporal behavior of the surface temperature. Then, the presence of defects is indicated by investigating the thermal gradient response on the surface of the inspection target with an IR camera. Controlled test conditions, such as heat source type, form, and amount of thermal energy, enable quantitative analysis and identification of defects [17]. The two primary common methods of active thermography are pulsed thermography (PT) and lock-in thermography (LIT). In PT, short and high-power thermal energy is applied to the surface of the target surface being inspected. In contrast, in LIT, sine-wave-modulated thermal energy is incident on the surface of the target, and phase delay and amplitude response are evaluated. An essential advantage of LIT is that it can characterize not only the defect's shape and size but also the defect's depth [14].

The mechanical behavior of composite structures can be affected by the presence of defects that may occur in the manufacturing process or in service conditions. In this regard, non-destructive testing, such as thermography, may be necessary to detect and characterize defects. Lock-in thermography is one of the most used active thermography techniques for inspecting composite materials [22]. Investigations on glass-reinforced polypropylene using lock-in thermography can be found in previous studies [7,23–26]. IRT was mainly conducted for the evaluation of internal inclusions of PP composites, detection of defects on the subsurface [27], evaluation of damage [28,29], detection of delamination [30,31], and

evaluation of manufacturing defects (porosity and misalignment) [32]. Previous studies have demonstrated the capability of lock-in thermography techniques to detect defects. However, only some defect conditions and limited heat source conditions were considered. Lock-in thermography results are obtained very differently depending on the excitation power of the external heating source, the excitation frequency band, the total thermal heating cycle, defect conditions, and the thermal properties of the test object. In other words, it is necessary to comprehensively consider the above major experimental factors, conduct experiments, and apply them to the field.

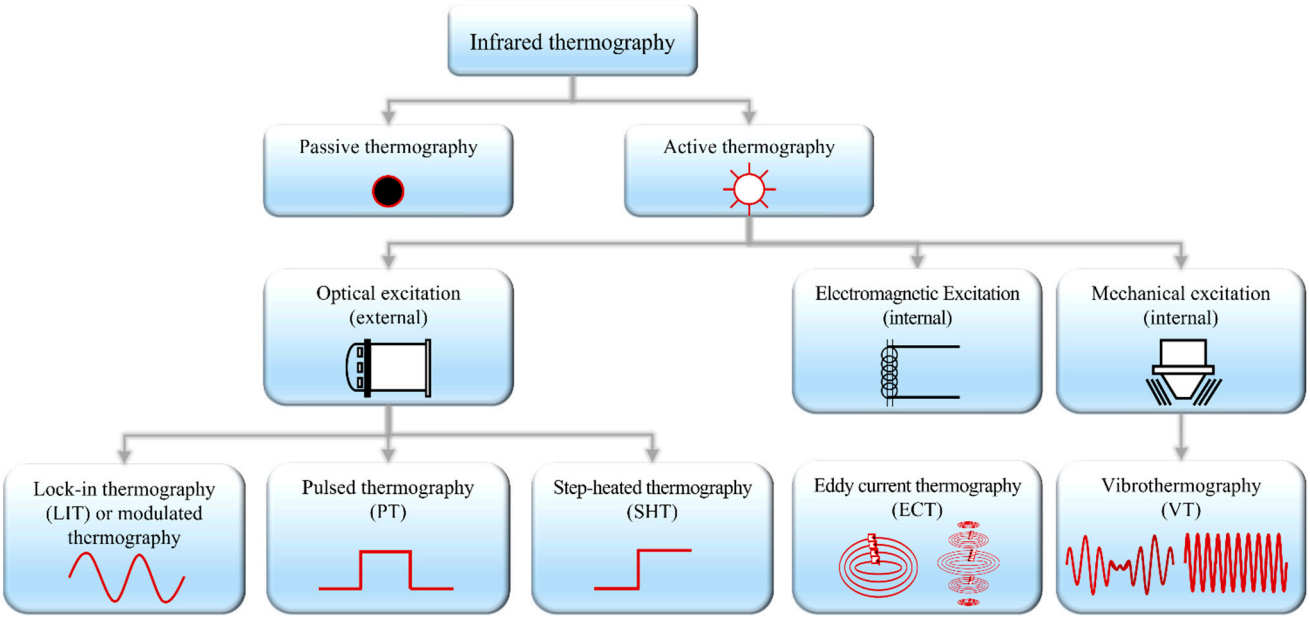


Figure 1. Classification of infrared thermographic testing approaches.

Therefore, in this study, an experimental investigation on the detection and non-destructive evaluation of various subsurface defects of polypropylene/glass fiber composites using multiple lock-in frequency modulated thermography is presented. The main objective of this study was to conduct quantitative evaluation of lock-in imaging on reference samples under different conditions of 24 defects of various sizes and depth. Fast Fourier transform (FFT) and harmonic approximation (HA) are the most widely used lock-in algorithms with high processing speed. Detectability was compared by FFT and HA. The second purpose was to quantitatively analyze the detectability of defects in terms of phase contrast and signal-to-noise ratio (SNR). Finally, the relationship between the SNR and the thermal image and its effect are presented. The rest of the paper is structured as follows. Section 2 provides information on basic concepts and algorithms related to this study. Subsequently, Section 3 provides information on samples and experimental methods applied in this study. Sections 4 and 5 present the experimental results and conclusion, respectively.

2. Theory

2.1. Lock-In Frequency Modulated Thermal Wave Imaging

Active thermography is a technique for recording a thermal response for a certain period of time by injecting external thermal energy into an object. Heat wave incident on the surface propagate to the material by diffusion. This wave will be reflected by defects placed on the object (surface cracks, subsurface defects, voids, and delamination) [17]. The presence of these defects affects the rate of diffusion of the damaged area to the surrounding area, which obeys the laws of thermodynamics. An IR camera can be used to

detect harmonic response patterns radiated on the surface of an object that is interfered by incident and reflected waves.

When thermal energy is incident on the opaque surface of the object, the object absorbs a portion of the incident energy and reflects a portion. The absorbed energy generates a localized heat flow on the sample surface. Time-dependent heat flow over time is defined by Fourier's one-dimensional thermal diffusion equation by Equation (1) [17,33]:

$$\frac{\partial^2 T(x,t)}{\partial x^2} = \frac{1}{\alpha} \cdot \frac{\partial T(x,t)}{\partial t} \tag{1}$$

where T is the temperature, k corresponds to the thermal conductivity, and α is expressed as material's thermal diffusivity ($\alpha = k/\rho c_p$); ρ resembles the density; c_p is specific heat capacity. If this heat source is modulated, a periodic heat flow is produced in the material. This sinusoidal heat flow in an object refers to a diffusion process that generates a periodic temperature distribution called a heat wave. Defects present in the object may be detected by analyzing the phase shift and amplitude damping on the surface with the infrared camera.

The periodical heat transfer through the semi-infinite (planar) body resulting thermal wave can be expressed by Equation (2) [34]:

$$T_{z,t} = A(z)\cos[\omega t - \varnothing(z)] = T_0 e^{-\frac{z}{\mu}} \cos\left[\omega t - \frac{2\pi z}{\lambda}\right] \tag{2}$$

where A(z) resembles the thermal amplitude; ω is expressed as an angular frequency ($\omega = 2\pi f$); $\varnothing(z)$ is the phase shift; t is the time; T_0 is an initial temperature change by incident thermal energy; z is the defect depth; λ is expressed as the thermal wavelength ($\lambda = 2\pi\mu$); and μ is the thermal diffusion length. The modulation frequency (f) and the thermal diffusivity can be expressed by Equation (3) [34]:

$$\mu = \sqrt{\frac{\alpha}{\pi f}} \tag{3}$$

From Equation (2), the phase shift ($\varnothing$) can be expressed as Equation (4), and it can be seen that it is related to the defect depth (z). By contrast, the amplitude ($A(z)$) can be expressed by Equation (5), and it can be seen that it is related to the initial temperature (T_0) [35,36].

$$\varnothing = \frac{z}{\mu} \tag{4}$$

$$A(z) = T_0 e^{-\frac{z}{\mu}} \tag{5}$$

2.2. Fast Fourier Transform (FFT)

The Fourier transform is a well-known and important tool in signal processing. In lock-in thermography (LIT), thermographic data is transformed from the time domain to the frequency domain using the one-dimensional discrete Fourier transform [37,38]. Discrete Fourier transform (DFT) can be used in any waveform to extract amplitude and phase angle from the transient signals. The DFT is applied to each pixel of the thermal sequence to compute amplitude and phase angle image sequences. Figure 2 shows the principle of amplitude and phase extraction by FFT.

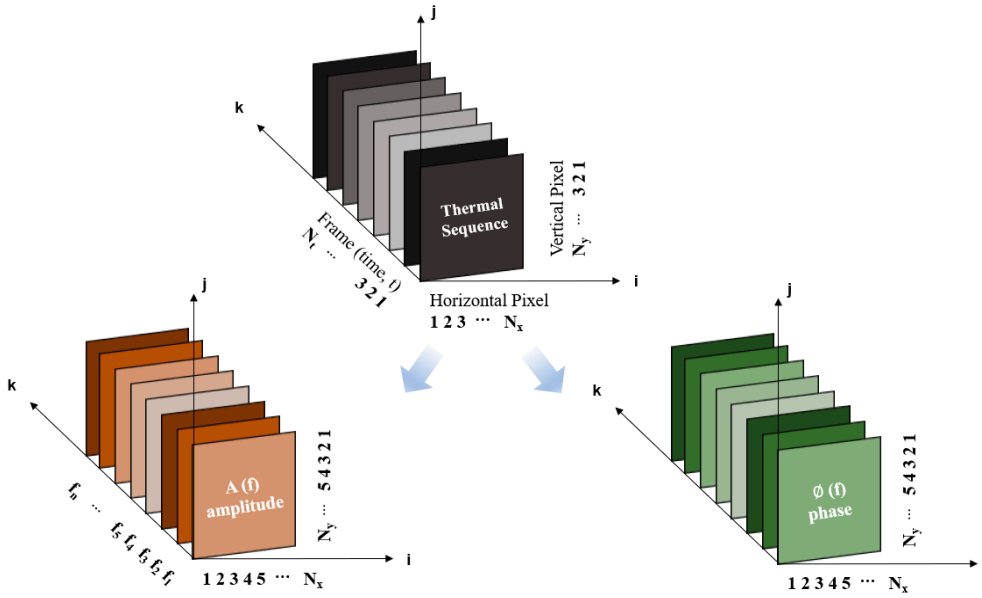


Figure 2. Principle of data acquisition and processing by fast Fourier transform.

The one-dimensional DFT can be expressed by Equation (6) [39,40]:

$$F_n = \Delta T \sum_{k=0}^{N-1} T(k\Delta T) \exp^{\frac{j2\pi nk}{N}} = Re_n + Im_n \quad (6)$$

where ΔT is the sampling interval; j2 is the imaginary number; N is the total number of thermography sequences; R_e and I_m are the real and the imaginary parts of the transform, respectively.

j2 = −1 is the imaginary number, *n* is the frequency increment (*n* = 0, 1, . . . , N), Δt is the sampling time interval, N is the total number of thermographic images, and Im_n and Re_n are the imaginary and real part of the transform, respectively. The lock-in frequency modulated thermographic data are converted into the frequency domain, and amplitude and phase angle images can be extracted. Real and imaginary parts of the complex transform are then applied to evaluate the amplitude (A_n) and phase angle ($\varnothing_n$) and can be expressed by Equations (7) and (8), respectively [41].

$$A_n = \sqrt{Re_n{}^2 + Im_n{}^2} \quad (7)$$

$$\varnothing_n = \tan^{-1}\left(\frac{Im_n}{Re_n}\right) \quad (8)$$

2.3. Harmonic Approximation (HA)

Harmonic approximation, commonly known as four-point method, approximates the Fourier transform based on the idea that only four data points per modulation cycle provide the correct phase and amplitude of a sinusoidal signal [42]. This method is fast, but only valid for sinusoidal stimulation. For the experimental LIT data, the four-point method and the Fourier transform computes the amplitude and phase angle data from the recorded temperature–time history of each pixel, then stored in the form of 2D matrices and converted to amplitude and phase images. If S_1, S_2, S_3, and S_4 are four equidistant thermal images, as shown in Figure 3, in a constant period, then the amplitude (A) and phase (∅) images can be expressed by Equations (9) and (10), respectively [43,44].

$$A = \sqrt{(S_1 - S_3)^2 + (S_2 - S_4)^2} \quad (9)$$

$$\varnothing = \tan^{-1}\left(\frac{S_1 - S_3}{S_2 - S_4}\right) \quad (10)$$

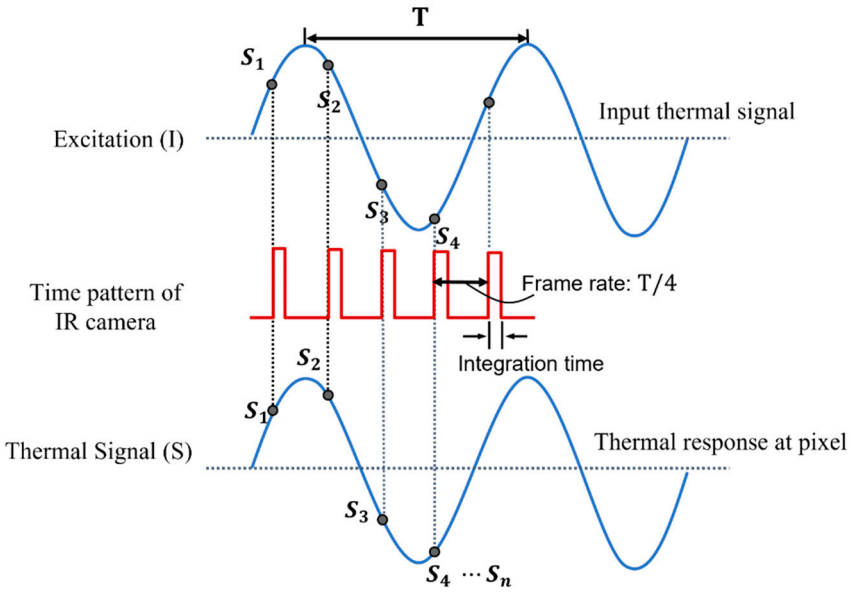


Figure 3. Principle of computation of thermal, amplitude, and phase images by using harmonic approximation.

3. Methods and Sample

3.1. Test Sample

In this study, a sample of PP-GF20 composite material was applied, and artificial defects composed of various types of defect sizes and depths were fabricated on the back side of the sample. A total of 8 specimens were prepared in the shape of a thin rectangular plate with a sample size of 100 mm × 180 mm × 3 mm (length × width × depth). These defects simulated defects that may occur during production or use of the product in aeronautical and automotive industries, such as damage and thinning.

Figure 4 shows the geometric information of the PP-GF20 composite sample, and Figure 5 shows the image of polypropylene/glass fiber composites on top view. As shown in Figure 4, a total of 8 samples were classified into 4 groups. First, in the case of group 1 (Figure 4a,b), they are samples considering the length, width, and depth of defects. Second, group 2 (Figure 4c,d) is samples considering the effect of length at a constant defect width (2 mm) and depth (1.8 mm). Third, group 3 (Figure 4e,f) is the samples considering the effect on width at a constant defect length (100 mm) and depth (1.8 mm). Lastly, group 4 (Figure 4g,h) is samples considering the effect of depth at a constant defect length (100 mm) and width (2 mm). Table 1 shows the dimensional values of information about the size and depth of artificial defects in the sample.

3.2. Experimental Procedures

Figure 6 shows a schematic diagram of the experimental setup for multiple lock-in frequency thermography applied in this study. Figure 7 shows a picture of the thermographic testing in progress of the PP-GF20 composites. As an external heat source, two 1 kW halogen lamps from Osram were irradiated with periodic heat waves on the sample surface. The halogen lamp was controlled by a function generator and power amplifier. The thermal response of the sample surface was acquired and recorded with infrared data through an infrared camera. In the excitation frequency range, the experiment was conducted while decreasing the frequency ranging from 1 to 0.01 Hz band. Tables 2 and 3 show the details of the experimental thermographic raw data considered for data analysis. The function generator (Agilent 33210A, Santa Clara, CA, USA) was used to produce periodic heat waves, and the infrared camera used to detect radiation from the surface of the sample was applied

with the FLIR SC655 model (640 × 480 pixels, 7.5~14 µm, Wilsonville, OR, USA). The sample can be placed on the infrared camera screen using a lens of 41.3 mm. The distance from the sample target surface to the IR camera is 1 m, and the distance to the halogen lamp is 1.5 m. Infrared images and temperature data were obtained using FLIR R&D commercial software. The frame of the camera was set to 50 frames per second for each frequency. The acquired data were processed through MATLAB 2022a software coding.

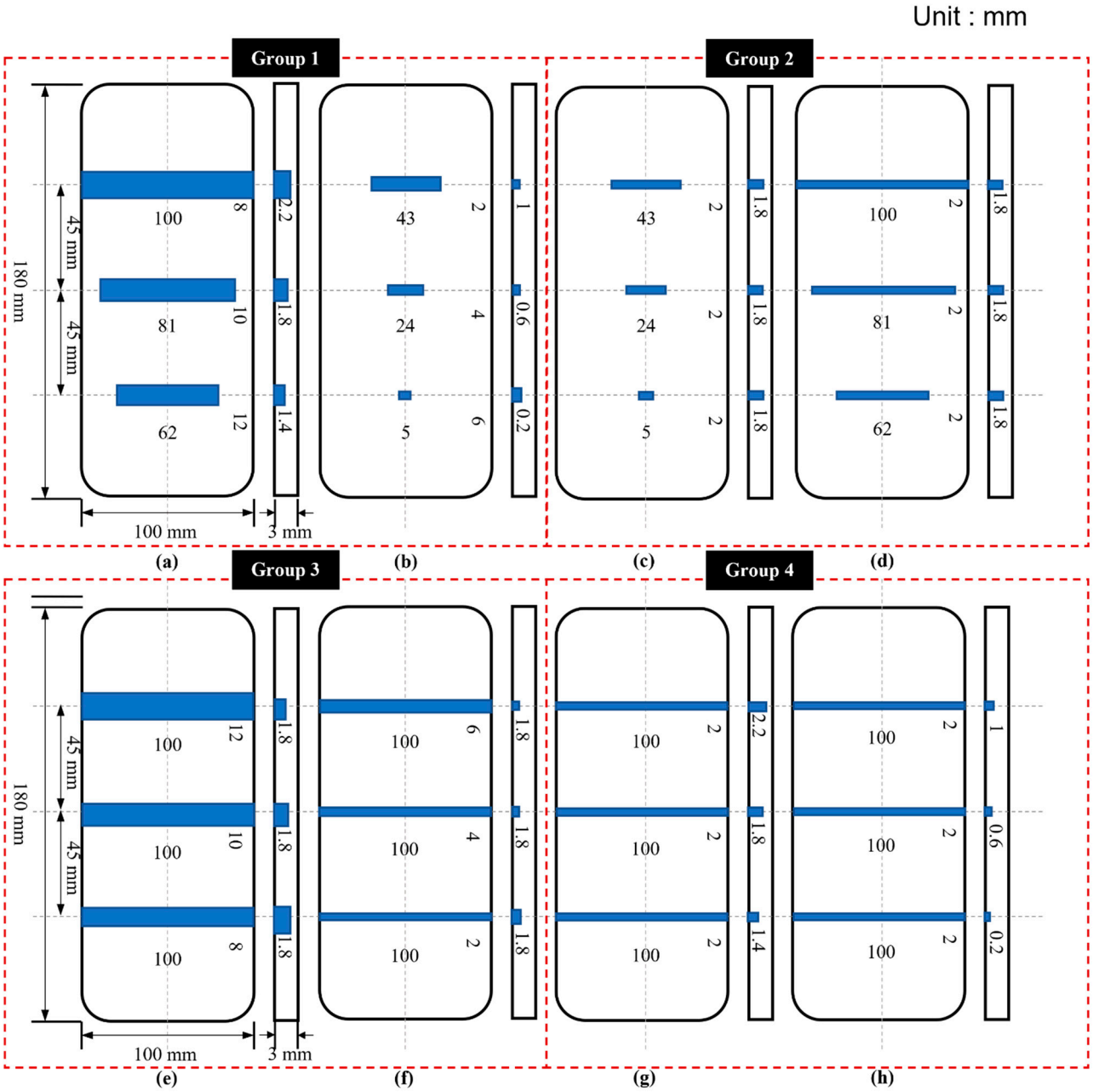


Figure 4. Schematic of the polypropylene composite sample considering various defect conditions, (**a**,**b**) according to composite defect (group 1); (**c**,**d**) according to length (group 2); (**e**,**f**) according to width (group 3); (**g**,**h**) according to depth (group 4).

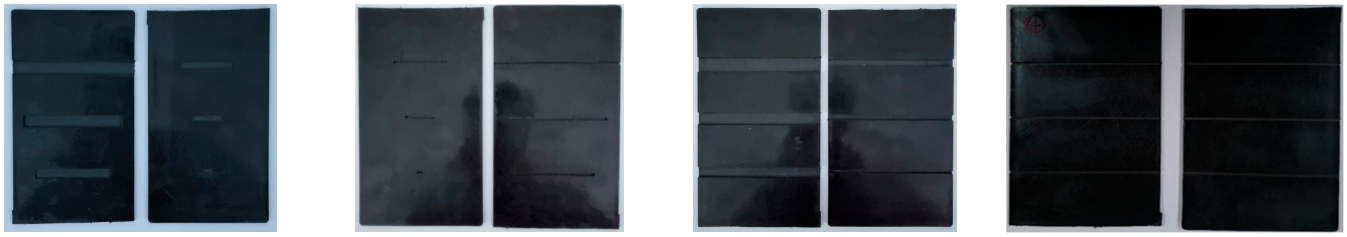


Figure 5. PP-GF20 plate as a test sample with artificial defects: (**a**) group 1, (**b**) group 2, (**c**) group 3, (**d**) group 4.

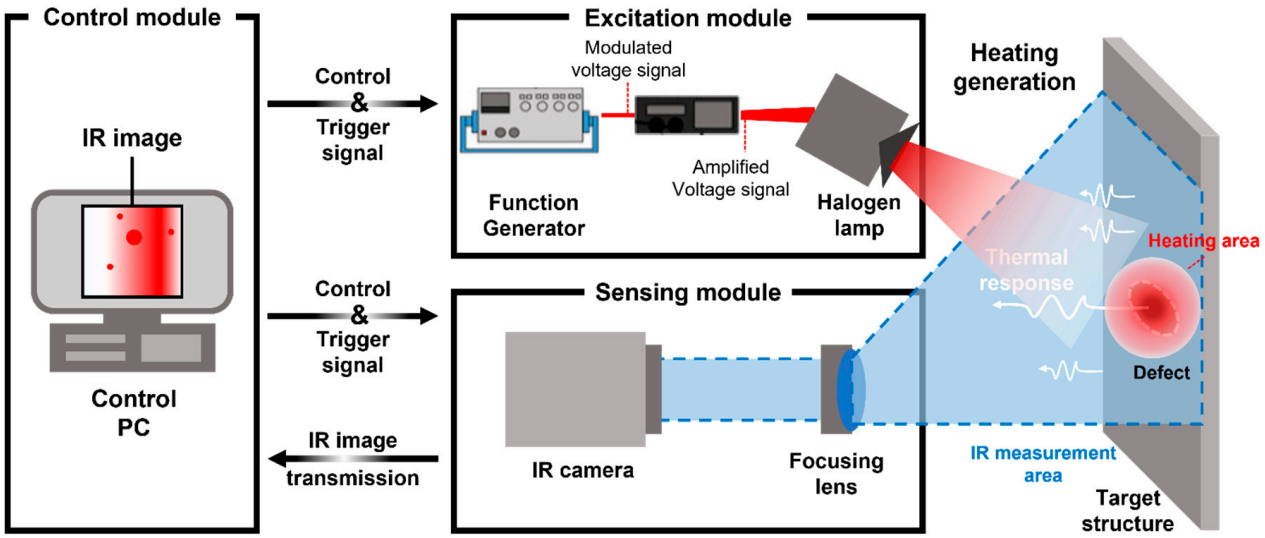


Figure 6. Experimental schematic of a lock-in frequency modulated thermal wave imaging system.

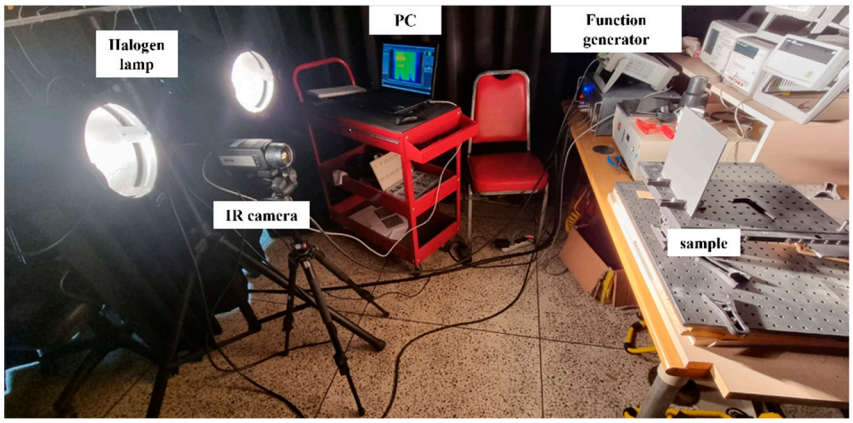


Figure 7. Picture undergoing thermographic testing on the sample.

Table 1. Classification of each defect and its dimensional value.

Defect ID.		Geometric Value (mm)		
Group	**No.**	**Length**	**Width**	**Depth**
1	1	5	2	0.2
	2	24	4	0.6
	3	43	6	1
	4	62	8	1.4
	5	81	10	1.8
	6	100	12	2.2
2	1	5	2	1.8
	2	24		
	3	43		
	4	62		
	5	81		
	6	100		
3	1	100	2	1.8
	2		4	
	3		6	
	4		8	
	5		10	
	6		12	
4	1	100	2	0.2
	2			0.6
	3			1
	4			1.4
	5			1.8
	6			2.2

Table 2. Details of experimental lock-in frequency modulated thermal wave imaging data.

Frequency (Hz)	Frame/ Cycle	Frame Interval	Frame Considered			
			1st	**2nd**	**3rd**	**4th**
1	60	15	75	90	105	120
0.2	300	75	375	450	525	600
0.1	600	150	750	900	1050	1200
0.05	1200	300	1500	1800	2100	2400
0.03	2000	500	2500	3000	3500	4000
0.01	6000	1500	7500	9000	10,500	12,000

Table 3. Details of thermographic raw data to be processed by HA.

Modulation Frequency (Hz)	Period (s)	Frame Rate (Hz)	Excitation Cycles (no.)	Total Frames (no.)	Frames Investigated (no.)
1	1	60	3	180	60
0.2	5			900	300
0.1	10			1800	600
0.05	20			3600	1200
0.03	33.33			6000	2000
0.01	100			18,000	6000

4. Results and Discussion

4.1. Defect Detection

The phase image results processed by HA and FFT for each defect group are shown in Figures 8–11. Figure 8 shows the defect detection image results of group 1. In all phase images of the HA and FFT, no defects were detected at 1 Hz.

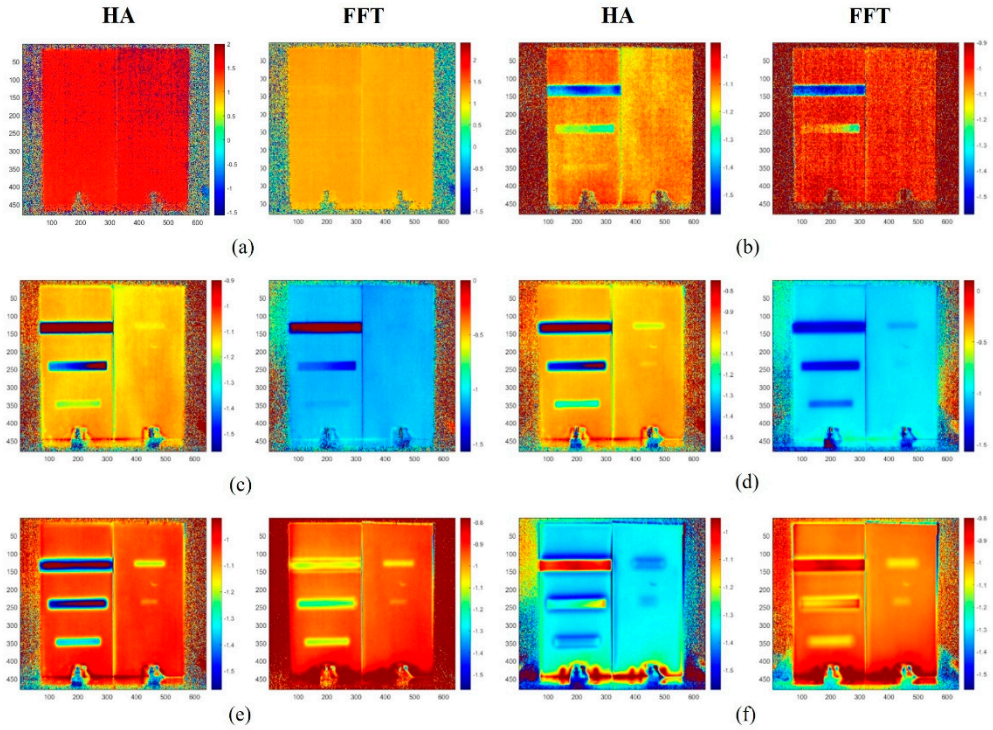


Figure 8. Processed images with HA and FFT algorithms for detecting defects in group 1 of samples at different modulation frequencies: (**a**) 1 Hz, (**b**) 0.2 Hz, (**c**) 0.1 Hz, (**d**) 0.05 Hz, (**e**) 0.03 Hz, and (**f**) 0.01 Hz.

However, from 0.5 Hz, defects are detected because the heat source provides enough energy to generate thermal contrast. In addition, the shape of the defect is somewhat blurred due to excessive heat transfer as it approaches the low modulation frequency of 0.01 Hz. Moreover, as the values of length, width, and depth for the samples decrease, the detectability decreases. For example, defects with a length of 100 mm, a width of 12 mm, and a depth of 2.2 mm were detected at all frequencies below the modulation frequency of 0.5 Hz. However, defects with a length of 5 mm, a width of 2 mm, and a depth of 0.2 mm were not detected in all modulation frequency bands. Figure 9 shows the defect detection image results of group 2 (according to defect length). In the case of the detection capability according to the defect length, all defects were detected in all modulation frequency bands of the HA and the FFT in the phase image, and the detectability started to drop from 0.2 Hz or higher and was not detected due to noise at 1.0 Hz. Figure 10 shows the defect detection image results of group 3 (according to defect width). The detectability according to the defect width showed a similar tendency to the group 2 results. Figure 11 shows the defect detection image results of group 4 (according to defect depth). In the case of detectability according to depth, it showed a different trend from groups 2 and 3. It can be seen that the depths of 2.2 mm, 1.8 mm, and 1.4 mm were detected from 0.2 Hz to 0.01 Hz and were not detected by noise at 1.0 Hz. In addition, it can be seen that the remaining 1 mm, 0.6 mm, and 0.2 mm depth defects start to be detected at 0.05 Hz or less. In other words, the lower the depth, the farther it is from the surface of the specimen, the more thermal energy must be provided with a lower frequency excitation to be detected.

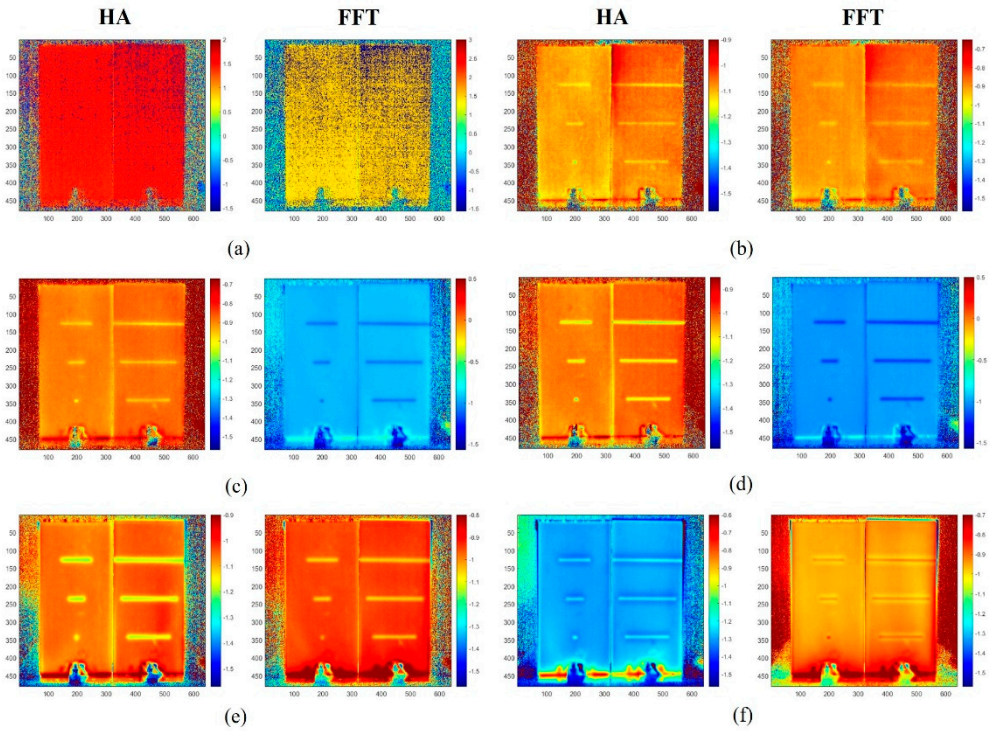


Figure 9. Processed images with HA and FFT algorithms for detecting defects in group 2 of samples at different modulation frequencies: (**a**) 1 Hz, (**b**) 0.2 Hz, (**c**) 0.1 Hz, (**d**) 0.05 Hz, (**e**) 0.03 Hz, and (**f**) 0.01 Hz.

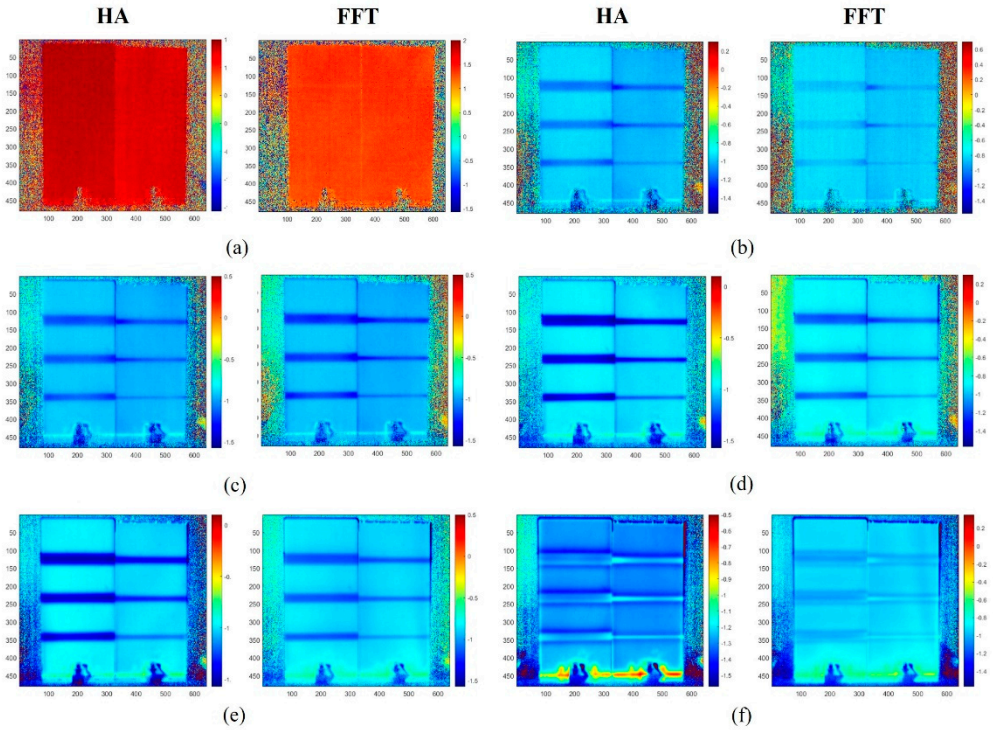


Figure 10. Processed images with HA and FFT algorithms for detecting defects in group 3 of samples at different modulation frequencies: (**a**) 1 Hz, (**b**) 0.2 Hz, (**c**) 0.1 Hz, (**d**) 0.05 Hz, (**e**) 0.03 Hz, and (**f**) 0.01 Hz.

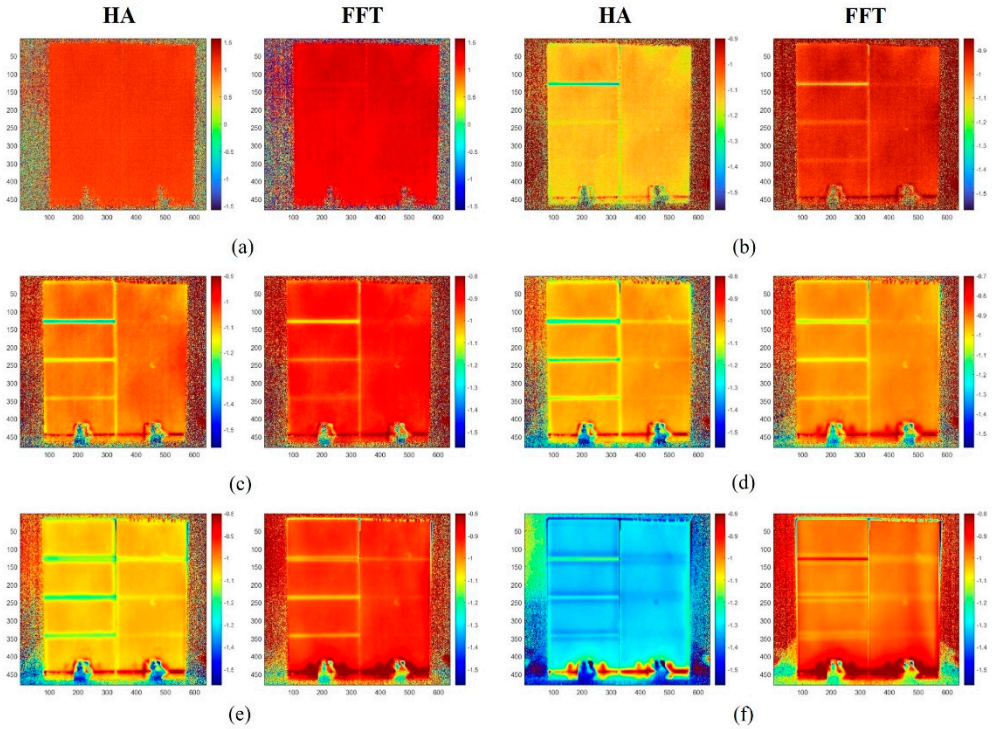


Figure 11. Processed images with HA and FFT algorithms for detecting defects in group 4 of samples at different modulation frequencies: (**a**) 1 Hz, (**b**) 0.2 Hz, (**c**) 0.1 Hz, (**d**) 0.05 Hz, (**e**) 0.03 Hz, and (**f**) 0.01 Hz.

4.2. Phase Contrast Trends

The phase contrast was calculated to analyze the quantitative change of the phase angle according to the lock-in modulation frequency, and the contrast analysis is defined as Equation (11) [34].

$$|\Delta C| = C_d - C_s \quad (11)$$

where C_d is the average value of phase angle in the defective area, and C_s is the average value of phase angle in the sound area. As shown in Figure 12, to determine the optimum frequency, two ROIs of 5 × 5 pixels (one at the center of defective area and another in the adjacent sound area) were considered. For analysis, cropping was performed except for unnecessary parts of the image. In addition, the relatively large and deep A6, A5, and A4 defects that were detected in the phase images were selected.

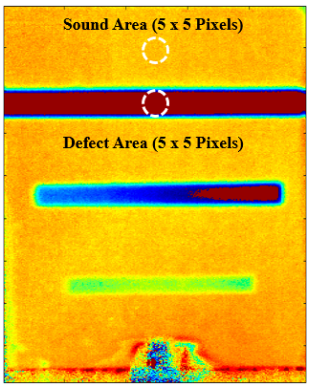


Figure 12. Representation of selected areas for phase contrast and signal to noise ratio (SNR) computation.

Figures 13 and 14 show the phase contrast of A6, A5, and A4 defects according to the HA and FFT algorithms. It can be seen that the phase contrast increases from 0.01 Hz to

0.05 Hz as the modulation frequency increases. Then, above 0.05 Hz, the phase contrast begins to decrease and approaches 0 (blind frequency) as it approaches 1 Hz. Therefore, phase detection can be estimated as the optimal frequency at 0.05 Hz. The maximum phase contrast of defect A6 in modulation frequency 0.05 Hz, HA was 0.8794 rad, FFT was 0.6208 rad.

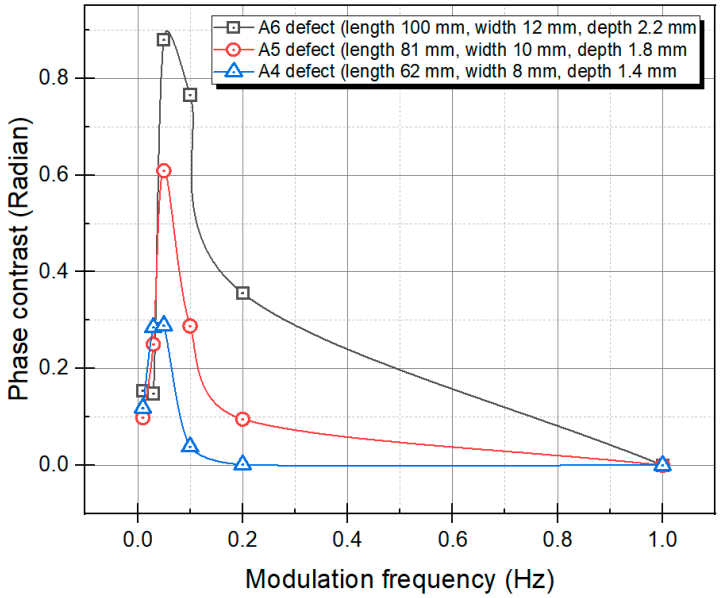


Figure 13. Phase contrast trend according to modulation frequency by HA.

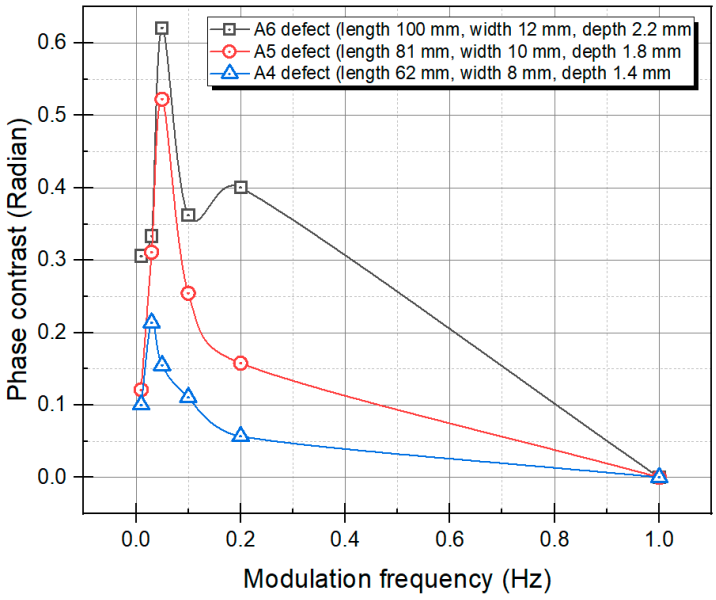


Figure 14. Phase contrast trend according to modulation frequency by FFT.

Table 4 shows the phase contrast results according to each algorithm for all samples and defects. In general, it can be seen that the size (length, width) of a defect is large, and the closer the defect is to the surface, the greater the phase contrast, so it is easy to detect the defect. In addition, it can be seen that defects having a phase contrast of about 0.2 rad or more quantitatively according to the modulation frequency are clearly distinguished from the sound area. For example, in the 0.05 Hz result of the HA algorithm, all group 3 defects were clearly detected. The phase contrast value of all group 3 defects in 0.05 Hz:C1 was 0.2275 rad, C2 was 0.2615 rad, C3 was 0.3714 rad, C4 was 0.3748 rad, C5 was 0.4372 rad,

and C6 was 0.4702 rad. On the other hand, when the phase contrast is less than 0.1 rad, a defect is detected, but the boundary between the sound area and the defect area is not cleared. For example, in the 0.2 Hz result of the FFT algorithm, all group 2 defects were clearly detected. The phase contrast value of all group 2 defects in 0.2 Hz:B1 was 0.0651 rad, B2 was 0.0501 rad, B3 was 0.0525 rad, B4 was 0.0478 rad, B5 was 0.0404 rad, and B6 was 0.05 rad.

Table 4. Phase contrast results for each algorithm according to the modulation frequency.

Defect Id.	Geometric Information (mm)			Phase Contrast |ΔC| (Radian)											
				HA						PPT					
	Length	Width	Depth	1 Hz	0.2 Hz	0.1 Hz	0.05 Hz	0.03 Hz	0.01 Hz	1 Hz	0.2 Hz	0.1 Hz	0.05 Hz	0.03 Hz	0.01 Hz
A1	5	2	0.2	-	-	-	-	-	-	-	-	-	-	-	-
A2	24	4	0.6	-	-	-	-	-	-	-	-	-	-	-	-
A3	43	6	1	-	-	-	-	-	-	-	-	-	-	-	-
A4	62	8	1.4	-	0.1187	0.2852	0.2889	0.0385	0.0016	-	0.0567	0.1106	0.1549	0.2137	0.1004
A5	81	10	1.8	-	0.0954	0.2879	0.6089	0.2502	0.0985	-	0.1578	0.2544	0.5225	0.3111	0.1212
A6	100	12	2.2	-	0.3558	0.7658	0.8794	0.1485	0.1547	-	0.4004	0.3624	0.6208	0.3335	0.3061
B1	5	2	1.8	-	0.1484	0.1751	0.0152	0.0850	0.1051	-	0.0651	0.0904	0.1625	0.0365	0.0986
B2	24			-	0.07502	0.1178	0.2281	0.1281	0.0879	-	0.0501	0.0657	0.1604	0.0875	0.0658
B3	43			-	0.0785	0.1279	0.2285	0.1201	0.9897	-	0.0525	0.0778	0.1602	0.0875	0.0640
B4	62			-	0.0804	0.1178	0.2185	0.1586	0.0898	-	0.0478	0.0652	0.1778	0.0880	0.0780
B5	81			-	0.1936	0.1839	0.2287	0.1158	0.0825	-	0.0404	0.0754	0.1898	0.0970	0.0778
B6	100			-	0.1578	0.1786	0.2205	0.1558	0.1802	-	0.0500	0.0983	0.1882	0.0972	0.0945
C1	100	2	1.8	-	0.1385	0.1848	0.2275	0.1952	0.1878	-	0.0458	0.0547	0.1822	0.8410	0.9214
C2		4		-	0.1353	0.1578	0.2618	0.2475	0.1915	-	0.0665	0.0875	0.2051	0.0748	0.0921
C3		6		-	0.1438	0.2175	0.3714	0.2956	0.1952	-	0.0947	0.1963	0.1851	0.0885	0.0785
C4		8		-	0.1431	0.2870	0.3748	0.2652	0.1889	-	0.9664	0.2520	0.3251	0.1954	0.1351
C5		10		-	0.1514	0.3187	0.4372	0.3025	0.1774	-	0.1686	0.2587	0.2247	0.1987	0.1425
C6		12		-	0.1573	0.3412	0.4702	0.4027	0.1702	-	0.1750	0.2305	0.2430	0.1741	0.1451
D1	100	2	0.2	-	-	-	0.0125	0.0105	0.0034	-	-	-	-	-	0.0088
D2			0.6	-	-	-	0.0145	0.0154	0.0066	-	-	-	-	0.0055	0.0014
D3			1	-	-	-	0.0420	0.0450	0.0070	-	-	-	0.0090	0.0091	0.016
D4			1.4	-	-	0.0456	0.0956	0.1368	0.041	-	0.0105	0.0156	0.0368	0.0806	0.0347
D5			1.8	-	0.1256	0.1912	0.2469	0.2400	0.1808	-	0.0554	0.0705	0.0944	0.0930	0.0896
D6			2.2	-	0.2654	0.2556	0.2202	0.1601	0.1934	-	0.0889	0.1584	0.1256	0.0746	0.1521

Note: '-' means that the defect is not detected in image.

4.3. Signal-to-Noise Trends

The SNR metric is used to differentiate the two regions of interest (ROI). The quantification of a defect is based on the information of two areas: the defective area and the reference or sound area. For the quantitative evaluation of each algorithm performance, the SNR of each defect for all the chosen modulation frequencies was calculated and compared. Two ROIs of 5 × 5 pixels were selected, one at the center of defective area and another in the adjacent sound area. ROI in the defective area will be considered as "signal" (DROI), and ROI in the sound area will be considered as "noise" (SROI). The SNR metric for a defect can be expressed by Equation (12) [45]:

$$\mathrm{SNR} = 20\log_{10}\left(\frac{|\mathrm{DROI}_{\mathrm{mean}} - \mathrm{SROI}_{\mathrm{mean}}|}{\sigma}\right) \quad (12)$$

where $\mathrm{SROI}_{\mathrm{mean}}$ is the arithmetic mean of the sound area; $\mathrm{DROI}_{\mathrm{mean}}$ is the arithmetic mean of the defective area; and σ is the standard deviation of the defective area.

To analyze the effect of the defect on the SNR of each parameter, the SNR values for all modulation frequencies were calculated by Equation (12). The SNR values for defects by each sample group were shown from Figures 15–17. Figure 15 shows the SNR values of group 2 in which the width and depth for defect are constant and the defect length is considered differently. As shown in Figure 15, the HA showed better SNR than FFT. The longer the defect length, the better the SNR value. In the case of a defect length of 100 mm at

0.05 Hz, the four-point method was excellent by about 25.1% with a difference of 7.7848 dB in SNR. Figure 16 shows the SNR values of group 3 in which the defect length and depth are constant, and the defect width is considered differently. In the case of group 3, HA also showed better SNR than FFT. On the other hand, the defect width has little effect on the SNR. When the defect width was 12 mm at 0.05 Hz, HA was excellent by about 22.4% with a difference of 6.971 dB in SNR. Figure 17 shows the SNR values of group 4 in which the defect length and width are constant, and the defect depth is considered differently. As shown in Figure 17, it can be seen that the deeper the defect depth and the closer to the surface, the better the SNR value. When the defect depth is 2.2 mm at 0.05 Hz, the HA was excellent by about 8.6% with a difference of 3.1072 dB in SNR. Comparing the phase difference and the SNR trend, a defect with a phase contrast of about 0.2 radian or more had an SNR of about 30 dB or more. The phase contrast value of all group 3 defect in 0.05 Hz:C1 was 38.7589 dB, C2 was 39.03 dB, C3 was 37.5052 dB, C4 was 39.3878 dB, C5 was 38.3682 dB, and C6 was 38.0906 dB.

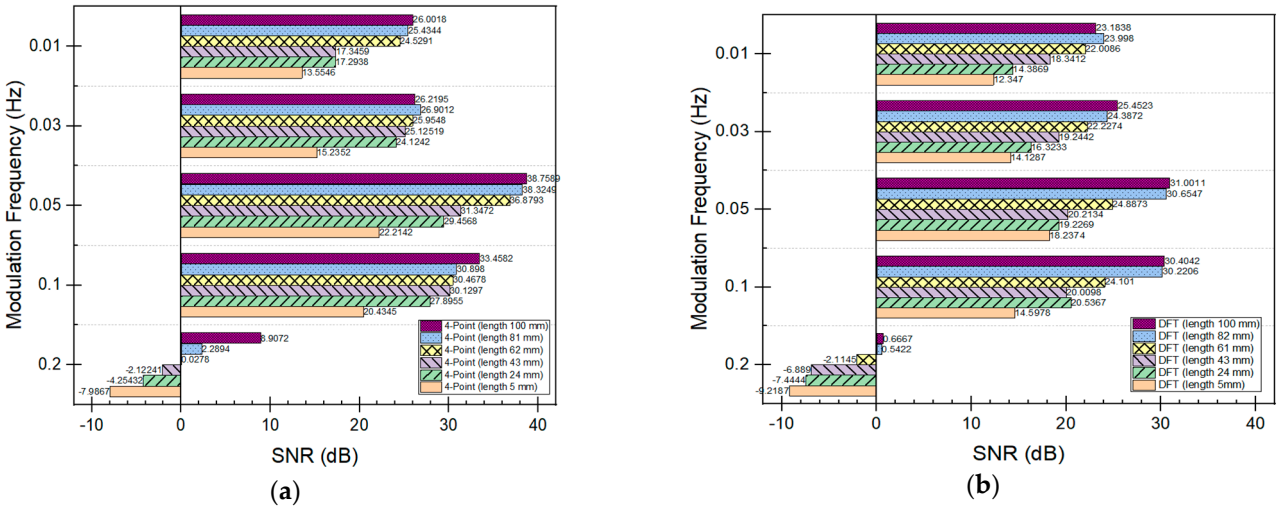


Figure 15. SNR value according to different defect length in sample group 2: (**a**) HA, (**b**) FFT.

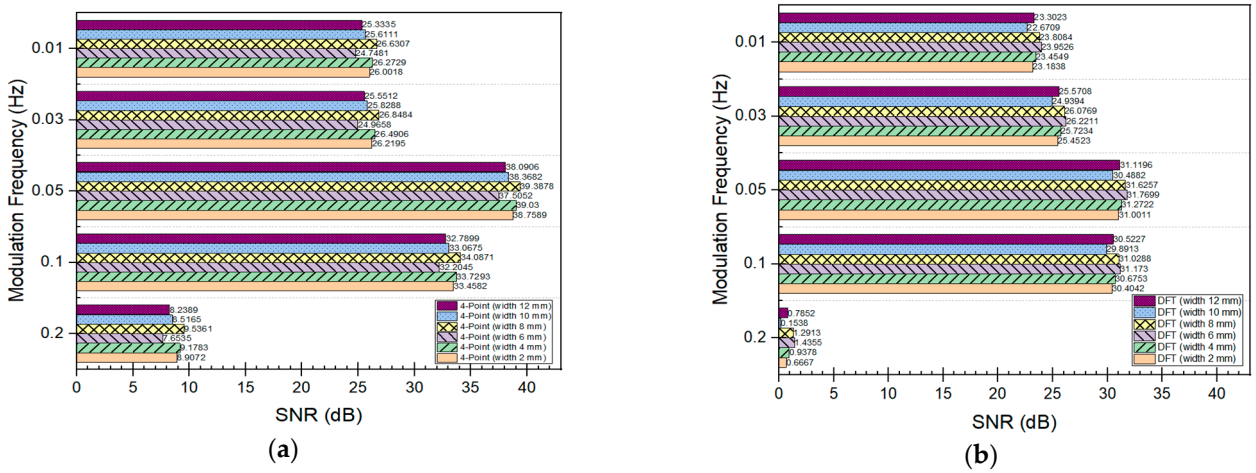


Figure 16. SNR value according to different defect width in sample group 3: (**a**) HA, (**b**) FFT.

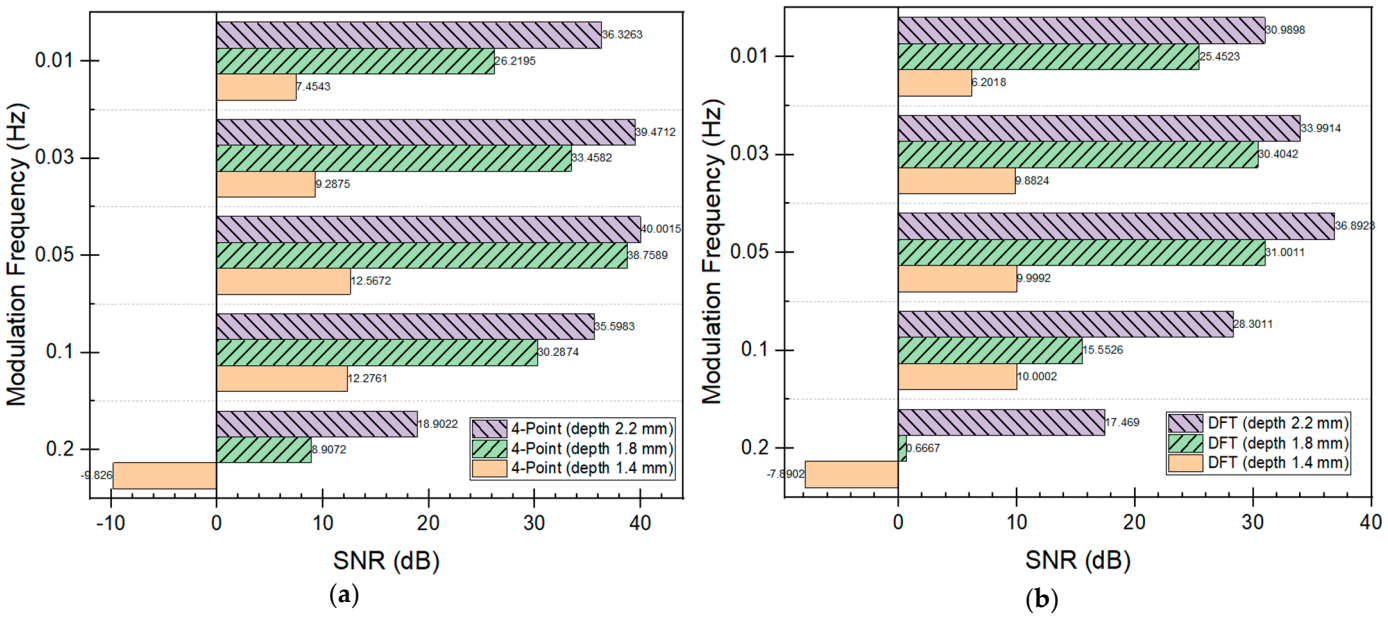


Figure 17. SNR value according to different defect depth in sample group 4: (**a**) HA, (**b**) FFT.

5. Conclusions and Future Works

In this study, a series of experiments were conducted to inspect subsurface defects in polypropylene/glass fiber (PP-GF) composites using the LIT. Various defect conditions were simulated for defects that may occur during product production and operation in the aerospace and automobile industries. Two representative multiple lock-in frequency modulated algorithms, viz., HA and FFT, were discussed. Phase images from raw data calculated by HA and FFT algorithms were considered. In the qualitative aspect, all algorithms showed appropriate and satisfactory results. However, shallow defects with a defect depth of 1 mm or less were hardly noticeable. Defect length and width hardly affect defect detection using LIT. On the other hand, the defect depth had a significant influence on the LIT detectability, and it has been proven that several tests are needed to select the optimal modulation frequency. That is, detectability tended to differ depending on the amount of energy of the total heat source provided. Defects with a depth of more than 1.4 mm showed the best phase contrast and SNR at a modulation frequency of 0.05 Hz, whereas defects below a defect depth of 1.4 mm showed poor results at all modulation frequencies. Additionally, the HA has superior detectability than FFT in terms of phase contrast and SNR. Finally, the defects showing sufficient phase contrast of 0.2 radian or more showed a correlation indicating an SNR of 30 dB or more.

Based on these results, in order to apply LIT to actual industrial sites, it is necessary to consider the dimension of defects and appropriate thermal excitation conditions. In this way, LIT can be utilized as a part of defect characterization in composites. However, in this study, the limited sample condition as a thin plate was applied, and investigation into real-field defect conditions is needed. In addition, improving advanced signal processing and image processing for deep defects will provide innovative solutions that can be used for defect characterization to enhance the reliability of composites.

Author Contributions: Conceptualization, W.K., Y.C. and R.S.; data curation, R.S.; formal analysis, R.S. and S.L.; funding acquisition, W.K.; investigation, W.K., Y.C., R.S. and S.L.; methodology, Y.C., R.S. and S.L.; project administration, W.K.; resources, W.K.; software, Y.C., R.S. and S.L.; supervision, W.K.; validation, W.K. and R.S.; visualization, R.S.; writing—original draft, Y.C. and R.S.; writing—review and editing, S.L. and W.K. All authors have read and agreed to the published version of the manuscript.

Funding: This work was supported by the National Research Foundation of Korea (NRF–2022R1A2C1011413) funded by the Korean Government, Ministry of Education, Science and Technology (MEST).

Institutional Review Board Statement: Not applicable.

Informed Consent Statement: Not applicable.

Data Availability Statement: Due to the nature of this research, participants of this study did not agree for their data to be shared publicly and data are only available upon reasonable request.

Conflicts of Interest: The authors declare no conflict of interests.

References

1. Kutz, M. *Mechanical Engineers' Handbook, Volume 1: Materials and Engineering Mechanics*; John Wiley & Sons: Hoboken, NJ, USA, 2015.
2. Senthilkumar, M.; Sreekanth, T.G.; Manikanta Reddy, S. Nondestructive Health Monitoring Techniques for Composite Materials: A Review. *Polym. Polym. Compos.* **2021**, *29*, 528–540. [CrossRef]
3. Koniuszewska, A.G.; Kaczmar, J.W. Application of Polymer Based Composite Materials in Transportation. *Prog. Rubber Plast. Recycl. Technol.* **2016**, *32*, 1–24. [CrossRef]
4. Giurgiutiu, V. *Structural Health Monitoring of Aerospace Composites*; Springer: Berlin/Heidelberg, Germany, 2015.
5. Tromaras, A.; Kappatos, V. Exploring Step-Heating and Lock-in Thermography NDT using One-Sided Inspection on Low-Emissivity Composite Structures for New Rail Carbodies. *Sensors* **2022**, *22*, 8195. [CrossRef] [PubMed]
6. Montanini, R.; Freni, F. Non-Destructive Evaluation of Thick Glass Fiber-Reinforced Composites by Means of Optically Excited Lock-in Thermography. *Compos. Part A Appl. Sci. Manuf.* **2012**, *43*, 2075–2082. [CrossRef]
7. Gholizadeh, S.; Gholizadeh, S. Impact Behaviours and Non-Destructive Testing (NDT) Methods in Carbon Fiber Composites in Aerospace Industry: A Review. *Authorea Prepr.* **2022**, 1–33. [CrossRef]
8. Khattak, M.A.; Mukhtar, A.; Shahid, I.S.; Sufian, M. A Review on Application of Non Destructive Techniques on Composites. *J. Adv. Res. Appl. Mech.* **2016**, *20*, 12–21.
9. Yan, Y.J.; Cheng, L.; Wu, Z.Y.; Yam, L.H. Development in Vibration-Based Structural Damage Detection Technique. *Mech. Syst. Signal Process.* **2007**, *21*, 2198–2211. [CrossRef]
10. Prade, F.; Schaff, F.; Senck, S.; Meyer, P.; Mohr, J.; Kastner, J.; Pfeiffer, F. Nondestructive Characterization of Fiber Orientation in Short Fiber Reinforced Polymer Composites with X-Ray Vector Radiography. *NDT E Int.* **2017**, *86*, 65–72. [CrossRef]
11. Miah, S.; Miah, M.H.; Hossain, M.S.; Ahsan, M.H. Study of the Homogeneity of Glass Fiber Reinforced Polymer Composite by using Neutron Radiography. *Am. J. Constr. Build. Mater.* **2018**, *2*, 22–28.
12. Boller, C.; Staszewski, W.J. Aircraft Structural Health and Usage Monitoring. In *Health Monitoring of Aerospace Structures*; Wiley: New York, NY, USA, 2004; pp. 29–73.
13. Masmoudi, S.; El Mahi, A.; Turki, S. Fatigue Behaviour and Structural Health Monitoring by Acoustic Emission of E-Glass/Epoxy Laminates with Piezoelectric Implant. *Appl. Acoust.* **2016**, *108*, 50–58. [CrossRef]
14. Chung, Y.; Lee, S.; Kim, W. Latest Advances in Common Signal Processing of Pulsed Thermography for Enhanced Detectability: A Review. *Appl. Sci.* **2021**, *11*, 12168. [CrossRef]
15. Yang, R.; He, Y. Optically and Non-Optically Excited Thermography for Composites: A Review. *Infrared Phys. Technol.* **2016**, *75*, 26–50. [CrossRef]
16. Osornio-Rios, R.A.; Antonino-Daviu, J.A.; de Jesus Romero-Troncoso, R. Recent Industrial Applications of Infrared Thermography: A Review. *IEEE Trans. Ind. Inform.* **2018**, *15*, 615–625. [CrossRef]
17. Maldague, X.P. *Nondestructive Evaluation of Materials by Infrared Thermography*; Springer Science & Business Media: Berlin, Germany, 2012.
18. Vollmer, M. Infrared thermal imaging. In *Computer Vision: A Reference Guide*; Springer: Berlin/Heidelberg, Germany, 2021; pp. 666–670.
19. Garrido, I.; Lagüela, S.; Otero, R.; Arias, P. Thermographic Methodologies used in Infrastructure Inspection: A review—Post-Processing Procedures. *Appl. Energy* **2020**, *266*, 114857. [CrossRef]
20. Meola, C. *Infrared Thermography Recent Advances and Future Trends*; Bentham Science Publishers: Sharjah, United Arab Emirates, 2012.
21. Ciampa, F.; Mahmoodi, P.; Pinto, F.; Meo, M. Recent Advances in Active Infrared Thermography for Non-Destructive Testing of Aerospace Components. *Sensors* **2018**, *18*, 609. [CrossRef]
22. D'Accardi, E.; Palumbo, D.; Galietti, U. A Comparison among Different Ways to Investigate Composite Materials with Lock-in Thermography: The Multi-Frequency Approach. *Materials* **2021**, *14*, 2525. [CrossRef]
23. Pickering, S.; Almond, D. Matched Excitation Energy Comparison of the Pulse and Lock-in Thermography NDE Techniques. *NDT E Int.* **2008**, *41*, 501–509. [CrossRef]
24. Chatterjee, K.; Tuli, S.; Pickering, S.G.; Almond, D.P. A Comparison of the Pulsed, Lock-in and Frequency Modulated Thermography Nondestructive Evaluation Techniques. *NDT E Int.* **2011**, *44*, 655–667. [CrossRef]
25. Palumbo, D. On the Thickness Quantification of Composite Materials by using Lock-in Thermography. *Materials* **2019**, *12*, 1185. [CrossRef]
26. Palumbo, D.; Tamborrino, R.; Galietti, U.; Aversa, P.; Tatì, A.; Luprano, V. Ultrasonic Analysis and Lock-in Thermography for Debonding Evaluation of Composite Adhesive Joints. *NDT E Int.* **2016**, *78*, 1–9. [CrossRef]

27. Banerjee, D.; Chattopadhyay, S.; Chatterjee, K.; Tuli, S.; Jain, N.; Goyal, I.; Mukhopadhyay, S. Non-Destructive Testing of Jute–polypropylene Composite using Frequency-Modulated Thermal Wave Imaging. *J. Thermoplast. Compos. Mater.* **2015**, *28*, 548–557. [CrossRef]
28. Li, Y.; Yang, Z.; Zhu, J.; Ming, A.; Zhang, W.; Zhang, J. Investigation on the Damage Evolution in the Impacted Composite Material Based on Active Infrared Thermography. *NDT E Int. Indep. Nondestruct. Test. Eval.* **2016**, *83*, 114–122. [CrossRef]
29. Khomenko, A.; Karpenko, O.; Koricho, E.; Haq, M.; Cloud, G.L.; Udpa, L. Theory and Validation of Optical Transmission Scanning for Quantitative NDE of Impact Damage in GFRP Composites. *Compos. Part B Eng.* **2016**, *107*, 182–191. [CrossRef]
30. Santulli, C. IR Thermography Study of the Effect of Moulding Parameters on Impact Resistance in E-Glass/Polypropylene Commingled Laminates. *NDT E Int.* **2002**, *35*, 377. [CrossRef]
31. Meola, C.; Boccardi, S.; Carlomagno, G.M.; Boffa, N.D.; Ricci, F.; Simeoli, G.; Russo, P. Impact Damaging of Composites through Online Monitoring and Non-Destructive Evaluation with Infrared Thermography. *NDT E Int. Indep. Nondestruct. Test. Eval.* **2017**, *85*, 34–42. [CrossRef]
32. Meola, C.; Carlomagno, G.M. Infrared Thermography to Evaluate Impact Damage in Glass/Epoxy with Manufacturing Defects. *Int. J. Impact Eng.* **2014**, *67*, 1–11. [CrossRef]
33. Fedala, Y.; Streza, M.; Sepulveda, F.; Roger, J.; Tessier, G.; Boué, C. Infrared Lock-in Thermography Crack Localization on Metallic Surfaces for Industrial Diagnosis. *J. Nondestr. Eval.* **2014**, *33*, 335–341. [CrossRef]
34. Meola, C.; Carlomagno, G.M. Recent Advances in the use of Infrared Thermography. *Meas. Sci. Technol.* **2004**, *15*, R27. [CrossRef]
35. Chung, Y.; Shrestha, R.; Lee, S.; Kim, W. Binarization Mechanism Evaluation for Water Ingress Detectability in Honeycomb Sandwich Structure using Lock-in Thermography. *Materials* **2022**, *15*, 2333. [CrossRef]
36. Lee, S.; Chung, Y.; Kim, C.; Shrestha, R.; Kim, W. Thermographic Inspection of CLP Defects on the Subsurface Based on Binary Image. *Int. J. Precis. Eng. Manuf.* **2022**, *23*, 269–279. [CrossRef]
37. Liu, J.; Yang, W.; Dai, J. Research on Thermal Wave Processing of Lock-in Thermography Based on Analyzing Image Sequences for NDT. *Infrared Phys. Technol.* **2010**, *53*, 348–357. [CrossRef]
38. Ibarra-Castanedo, C.; Maldague, X. Pulsed Phase Thermography Reviewed. *Quant. Infrared Thermogr. J.* **2004**, *1*, 47–70. [CrossRef]
39. Olbrycht, R.; Więcek, B.; Gralewicz, G.; Świątczak, T.; Owczarek, G. Comparison of Fourier and Wavelet Analyses for Defect Detection in Lock-in and Pulse Phase Thermography. *Quant. InfraRed Thermogr. J.* **2007**, *4*, 219–232. [CrossRef]
40. Chrysafi, A.P.; Athanasopoulos, N.; Siakavellas, N.J. Damage Detection on Composite Materials with Active Thermography and Digital Image Processing. *Int. J. Therm. Sci.* **2017**, *116*, 242–253. [CrossRef]
41. Chung, Y.; Shrestha, R.; Lee, S.; Kim, W. Thermographic Inspection of Internal Defects in Steel Structures: Analysis of Signal Processing Techniques in Pulsed Thermography. *Sensors* **2020**, *20*, 6015. [CrossRef]
42. Shrestha, R.; Choi, M.; Kim, W. Thermographic Inspection of Water Ingress in Composite Honeycomb Sandwich Structure: A Quantitative Comparison among Lock-in Thermography Algorithms. *Quant. InfraRed Thermogr. J.* **2021**, *18*, 92–107. [CrossRef]
43. Busse, G.; Gleiter, A.; Spiessberger, C. NDE using Lockin-Thermography: Principle and Recent Developments. In *Nondestructive Testing of Materials and Structures*; Springer: Dordrecht, The Netherlands, 2013; pp. 627–632.
44. Shrestha, R.; Park, J.; Kim, W. Application of Thermal Wave Imaging and Phase Shifting Method for Defect Detection in Stainless Steel. *Infrared Phys. Technol.* **2016**, *76*, 676–683. [CrossRef]
45. Shrestha, R.; Kim, W. Non-Destructive Testing and Evaluation of Materials using Active Thermography and Enhancement of Signal to Noise Ratio through Data Fusion. *Infrared Phys. Technol.* **2018**, *94*, 78–84. [CrossRef]

Disclaimer/Publisher's Note: The statements, opinions and data contained in all publications are solely those of the individual author(s) and contributor(s) and not of MDPI and/or the editor(s). MDPI and/or the editor(s) disclaim responsibility for any injury to people or property resulting from any ideas, methods, instructions or products referred to in the content.